

WHAT SETS THE LINE PROFILES IN TIDAL DISRUPTION EVENTS?

NATHANIEL ROTH¹ AND DANIEL KASEN^{2,3,4}

¹Department of Astronomy and Joint Space-Science Institute, University of Maryland, College Park, MD 20742, USA

²Department of Physics, University of California, Berkeley, CA 94720, USA

³Department of Astronomy and Theoretical Astrophysics Center, University of California, Berkeley, CA 94720, USA

⁴Nuclear Science Division, Lawrence Berkeley National Laboratory, Berkeley, CA 94720, USA

ABSTRACT

We investigate line formation in gas that is outflowing and optically thick to electron scattering, as may be expected following the tidal disruption of a star by a super-massive black hole. Using radiative transfer calculations, we show that the optical line profiles produced by expanding TDE outflows are most likely primarily emission features, rather than the P-Cygni profiles seen in most supernova spectra. This is a result of the high line excitation temperatures in the highly irradiated TDE gas. The outflow kinematics cause the emission peak to be blueshifted and to have an asymmetric red wing. Such features have been observed in some TDE spectra, and we propose that these may be signatures of outflows. We also show that non-coherent scattering off of hot electrons can broaden the emission lines by $\sim 10000 \text{ km s}^{-1}$, such that in some TDEs the line width may be set by the electron scattering optical depth rather than the gas kinematics. The scattering broadened line profiles produce distinct, wing-shaped profiles that are similar to those observed in some TDE spectra. The narrowing of the emission lines over time in these observed events may be related to a drop in density rather than a drop in line-of-sight velocity.

Keywords: black hole physics – line: formation – galaxies: nuclei – methods: numerical – radiative transfer

1. INTRODUCTION

Wide-field surveys are discovering a growing number of TDEs at optical wavelengths (van Velzen et al. 2011; Gezari et al. 2012; Arcavi et al. 2014; Holoien et al. 2014, 2016b; Blagorodnova et al. 2017; Hung et al. 2017). Despite the abundance of data, the origin of the optical emission remains unclear. The observations suggest that the optical radiation is produced from a region many times larger than the tidal disruption radius. A number of explanations have been proposed to explain this extended emission region: the formation of a quasi-static reprocessing envelope surrounding an accretion disk (Loeb & Ulmer 1997; Bogdanović et al. 2004; Guillochon et al. 2014), the ejection of a quasi-spherical outflow of stellar debris (Strubbe & Quataert 2009; Lodato & Rossi 2011; Miller 2015; Metzger & Stone 2016), or collisions occurring in the stellar debris streams falling back to the black hole (Kochanek 1994; Piran et al. 2015; Krolik et al. 2016; Jiang et al. 2016; Bonnerot et al. 2017).

Optical and UV spectra, when available, can provide

a wealth of information about the kinematics and conditions in the emitting gas that may allow us to test these hypotheses. However, interpreting the spectra is challenging because of the high gas densities and uncertain geometry (Gaskell & Rojas Lobos 2014; Guillochon et al. 2014; Strubbe & Murray 2015). A previous study (Roth et al. 2016, hereafter R16) presented detailed radiative transfer calculations of the spectra from an optically thick, spherical TDE envelope. However, these calculations assumed that electron scattering was coherent, and that the motion of the envelope gas was turbulent rather than outflowing. The simplifications prevented an analysis of how the kinematics and thermal properties of the line-emitting gas shape the line profiles. A number of fundamental questions regarding the spectra of TDEs remain to be addressed:

1) Many models of the optical emission for TDEs argue that the optical emission is produced in a nearly spherical outflow of stellar debris ejected with velocities $\sim 10^4 \text{ km s}^{-1}$. Indeed, radio detections of some TDE provide evidence of non-relativistic outflows (Alexander et al. 2015, 2017) (but see van Velzen et al. 2016; Krolik et al. 2016, for alternative interpretations). In analogy to supernovae, one might expect such outflows would

produce P-Cygni spectral line profiles, with both absorption and emission components. In contrast, TDEs generally show pure emission profiles, with the possible exceptions of PTF-11af (Chornock et al. 2014), iPTF-16fnlBrown2017-2, and ASASSN-15lh (Dong et al. 2015; Leloudas et al. 2016; Margutti et al. 2016) (although for the latter a TDE identification is debated). It thus unclear whether the line profiles of TDEs are consistent with outflows and, if so, why TDE spectra differ qualitatively from those of supernovae.

2) While the emission lines in TDEs generally have widths corresponding to velocities of $\sim 10^4$ km s $^{-1}$, there is a large spread in widths between individual events (Figure 15 of Hung et al. 2017). In some cases the line widths narrow over time while the luminosity drops (Holoien et al. 2016b,a; Blagorodnova et al. 2017; Brown et al. 2017), which is opposite to the behavior seen in reverberation mapping of quasars (Holoien et al. 2016a). It is unclear how the line widths in TDEs are related to the kinematics or other physics in the emitting gas.

3) In a number of TDEs, the early spectra show emission lines with blueshifted centroids (Holoien et al. 2014; Arcavi et al. 2014; Holoien et al. 2016a). There is also evidence of a line asymmetry in these events, with the emission extending farther to the red side of line than to the blue. In all cases when multi-epoch spectroscopy is available, the centroid moves closer to the host rest frame over time, and the line becomes more symmetric. One potential explanation (Gezari et al. 2015; Brown et al. 2017) for the blueshifted component of the He II $\lambda 4686$ line is that it is a blend of C III and N III emission (Bowen fluorescence). While this seems like a promising explanation in some cases, it cannot explain blueshifts of H α , and it may not provide blue enough emission to match some of the observations.

In this paper, we use radiative transfer models to study the fundamental physics of TDE line formation and address the above questions. We find that optically thick TDE outflows likely produce H and He lines with pure emission (not P-Cygni) profiles, similar to what is seen in observed spectra. The lack of line absorption is a result of the high line source function realized in the strongly irradiated TDE gas. We show that typical signatures of an outflow include a blueshifted line emission peak, and an asymmetric, extended red wing – both features that have been seen in the spectra of observed TDEs. In addition, we show that the line widths and their time evolution can be significantly affected by non-coherent (Compton) electron scattering; thus, in some TDEs the line widths may be related to thermal broadening in addition to (or rather than) the bulk kinematics of the line-emitting gas.

In Section 2, we describe the basic features of our model setup. Then, to provide intuition into the physics

shaping line formation in TDEs, we consider simple and parametrized calculations. Section 3 demonstrates how the line source function controls whether or not a P-Cygni or pure emission line profile will be generated in an outflow. Section 4 illustrates how repeated non-coherent scattering of photons off of thermal electrons can broaden an emission line, and applies this idea to fit the line profiles of ASASSN-14li. In Section 5 we move on to more detailed calculations combining the aforementioned effects. We explore how H α lines may be shaped by the hydrodynamic parameters, and present a fit to ASASSN-14ae. We also discuss how the He II to H α line strengths should evolve. We summarize our conclusions and characterize the limitations of our work in Section 6.

2. MODEL SETUP

We perform radiative transfer calculations in spherical symmetry using an adapted version of *Sedona*, a Monte Carlo radiative transfer code (Kasen et al. 2006; Roth & Kasen 2015). We consider gas that is distributed with a density profile $\rho(r) \propto r^{-2}$ between an inner radius r_{in} and outer radius R . The gas is outflowing with a velocity profile $v(r)$ specified below. We take the gas properties to be time-independent, appropriate for the regime where the radiation diffusion time is small compared to the timescale over which the gas properties change. More detailed calculations would solve for the time-dependent hydrodynamics of the envelope density and velocity structure, along with the consequent time-dependent radiation properties.

We model spectra in a wavelength interval surrounding a single line of interest, in this case the H α transition in hydrogen (though the qualitative features of line formation we discuss likely apply to other optical lines of interest). In the Monte Carlo calculation, continuum photon packets are emitted from a inner, absorbing boundary at radius r_{th} , representing the radius of thermalization of the continuum. We specify the luminosity of the continuum emission at r_{th} , and take the continuum spectrum to be flat (constant in F_λ) given the narrow wavelength interval modeled. Photon packets are further emitted and absorbed at each location within the gas in accordance with the line opacity and source function. In our simplified calculations, we set these two quantities parametrically, while in our more detailed models we derive them by solving the non-LTE rate equations for the ionization and excitation states of the gas under statistical equilibrium (see Appendix A). We tally the escaping packets from both the line and the continuum to generate the observed spectrum.

3. WHY NOT A P-CYGNI PROFILE? THE ROLE OF THE LINE SOURCE FUNCTION

We first consider simple models that help explain TDE line profiles. We consider an expanding outflow with a homologous velocity profile

$$v(r) = v_{\text{sc}} \frac{r}{R}, \quad (1)$$

where v_{sc} is the velocity at the outer boundary R . For an atomic line with intrinsic width given by the Doppler velocity v_{D} , photons interact with the gas in the so-called resonance region which for a homologous outflow has a physical size

$$\Delta r = v_{\text{D}} \left(\frac{dv}{dr} \right)^{-1} = \frac{v_{\text{D}}}{v_{\text{sc}}} R. \quad (2)$$

In outflows with strong velocity gradients ($v_{\text{sc}} \gg v_{\text{D}}$), Δr is small compared to the scales over which the gas properties vary, and the Sobolev approximation (Sobolev 1947) can be used to calculate the resulting line profile (e.g. Jeffery & Branch 1990).

The optical depth integrated across the resonance region at some radius r is a local quantity, $\tau_s(r)$, called the Sobolev optical depth. The profile of a line is determined by $\tau_s(r)$ and the line source function, given by

$$S_{\lambda} = \frac{2hc^2}{\lambda^5} \frac{1}{\exp\left(\frac{hc}{\lambda_{\text{line}} k_B T_{\text{ex}}}\right) - 1}, \quad (3)$$

where T_{ex} is referred to as the line excitation temperature (Jefferies & Thomas 1958). T_{ex} only corresponds to a true thermodynamic temperature when the atomic level populations are in local thermodynamic equilibrium; more generally

$$\exp\left(\frac{hc}{\lambda_{\text{line}} k_B T_{\text{ex}}}\right) = \frac{g_2 n_1}{g_1 n_2} \quad (4)$$

where n_1, n_2 are the level populations and g_1, g_2 the statistical weights of the lower and upper levels (respectively) of the atomic transition.

Line formation in rapidly expanding outflows is familiar from studies of supernovae and stellar winds, and is illustrated in the schematic Figure 1. In the simple, heuristic picture, continuum flux is emitted from the surface of a sharp photosphere into tenuous line forming gas. The gas on the sides of the photosphere produces a line emission feature that peaks at the line center wavelength. The gas in front of the photosphere – which is moving towards the observer – obscures the continuum flux and, in the classic P-Cygni profile, produces a blueshifted absorption feature.

The absorption component of the P-Cygni profile shown in Figure 1 is only produced when the gas in the “absorption region” absorbs more than it emits. This occurs when T_{ex} is less than the brightness temperature, T_{bb} , of the photosphere. In the common assumption of resonance line scattering (where every line absorption is

immediately followed by emission via the same atomic transition) the source function equals the mean intensity of the local radiation field, and $T_{\text{ex}} < T_{\text{bb}}$ due to the geometrical dilution of the continuum radiation emergent from the photosphere.

In highly irradiated TDE outflows, however, it is possible for T_{ex} to deviate from the resonant scattering value. A self-consistent calculation would require that we simultaneously solve the non-LTE rate equations coupled with the radiative transfer equation. The former determine the emissivity and opacity of each line, while the latter determines quantities such as photoionization rates and mean radiative intensities at line wavelengths $\bar{J}_{\lambda, \text{line}}$, which enter into the non-LTE equations that determine the line emissivities and opacities.

Here, to illustrate the diversity of line profiles, we present transport models that ignore electron scattering and use a simple parametrization for T_{ex} . We choose T_{ex} to vary linearly with the gas column density such that it is equal to some specified $T_{\text{ex, out}}$ at R and 10 times that value at r_{th} . Such behavior is consistent with the line source function we find in more detailed NLTE calculations (see Section 5).

As a fiducial model, we choose $r_{\text{in}} = 10^{14}$ cm, $R = 10^{15}$ cm, $v_{\text{sc}} = 10^4$ km s $^{-1}$, and an envelope mass of $0.25 M_{\odot}$ (which gives $\rho(r_{\text{in}}) = 4.32 \times 10^{-12}$ g cm $^{-3}$). We set $v_D = 400$ km s $^{-1}$, $r_{\text{th}} = 3 \times 10^{14}$ cm and $\kappa = 0.03$ cm 2 g $^{-1}$, in this case constant with radius. For the source function described above, the choice for the absolute strength of the continuum flux does affect the emission or absorption properties of the line, and we choose to set it so that the luminosity is 2.5×10^{38} erg s $^{-1}$ Å $^{-1}$.

The resulting model line profiles are shown in Figure 2. For $T_{\text{ex, out}} = 2000$ K, the line profile is very similar to that of resonant scattering. Reducing $T_{\text{ex, out}}$ to 1000 K produces a line with prominent blueshifted absorption and very little emission. Raising $T_{\text{ex, out}}$ to 5000 K makes the blueshifted absorption shallower and extended over a smaller range of wavelengths.

For $T_{\text{ex, out}} = 10000$ K the line appears entirely in emission. It turns out that this choice is close to the line source function we compute in Section 5 following the more detailed NLTE procedure described in Appendix A. The high values of T_{ex} arise in the full calculation because of the high radiative luminosity emanating from the inner TDE engine, the limited spatial extent of the line-emitting gas, and the high scattering depth that traps the radiation and raises its mean intensity compared to the free-streaming case.

The line profiles in Figure 2 show a fairly flat peak with a extending to the blue of the line rest wavelength. For homologous expansion, all emission and absorption at a given wavelength corresponds to gas on a $z = \text{constant}$ plane (see coordinate system labels on the Fig-

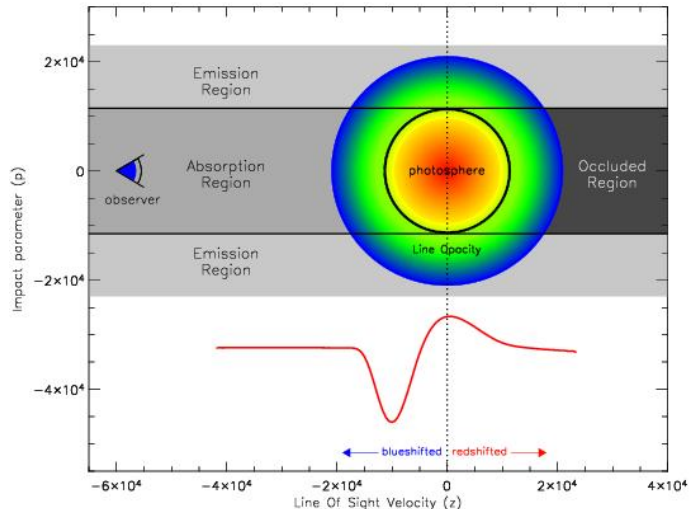


Figure 1. Schematic of line formation in an expanding atmosphere. For TDE atmospheres, the line source function can be large enough that the gas in the “absorption region” emits more than it absorbs. In this case the line will produce a pure emission profile.

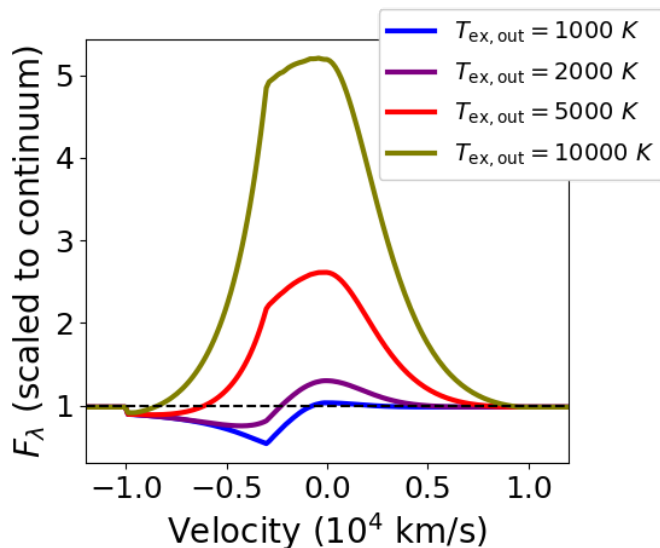


Figure 2. A demonstration of how the line excitation temperature T_{ex} (a measure of the line source function) affects line profiles in an expanding atmosphere, in the simplified case of no electron scattering. Here T_{ex} is set in simple parametrized fashion, ranging from the specified value at the outer radius to 10 times that value at the inner photosphere for the continuum. A classical P-Cygni profile, with blueshifted absorption and redshifted emission tail, is generated for an intermediate value of T_{ex} . For lower values of T_{ex} , the profile displays prominent blueshifted absorption with little corresponding emission. For higher values of T_{ex} , the line appears entirely in emission. In this figure the maximum velocity of the gas is $v_{\text{sc}} = 10^4 \text{ km s}^{-1}$, and the velocity at the continuum thermalization depth is $v_{\text{th}} = -3 \times 10^3 \text{ km s}^{-1}$.

ure 1). For $z > r_{\text{th}}$, the plane fully covers the continuum

photosphere, but for $z < r_{\text{th}}$ the plane cuts through the photosphere so that only its edges are blocked. Therefore we see a shoulder at the approaching velocity of the photosphere $v_{\text{th}} \equiv -v_{\text{sc}} r_{\text{th}}/R$.

While P-Cygni profiles were not generated for the H α and He II line profiles calculated below, other lines such as those from highly ionized carbon and nitrogen, would potentially display blueshifted absorption in the same environment, as has sometimes been seen in the UV spectra of TDEs (Chornock et al. 2014; Blagorodnova et al. 2017), where the line source functions may be closer to resonant scattering.

4. THE ROLE OF NON-COHERENT ELECTRON SCATTERING IN SETTING LINE WIDTHS AND LINE-NARROWING

In addition to the kinematic effects just discussed, spectral lines can be broadened by multiple scatterings of photons by electrons (Dirac 1925; Münch 1948; Chandrasekhar 1950). Electrons in random thermal motion have velocities $v_e \approx \sqrt{k_B T_e / m_e}$, where T_e and m_e are respectively the electron temperature and mass. Photons with energies that are small compared to the electron rest energy pick up Doppler shift factors of order v_e/c in each scattering event. After N scattering events, a photon has undergone an effective diffusion process in wavelength space such that the line photon broadens by a factor of $\sim \sqrt{N} v_e/c$ (note that this behavior changes for large enough N and large enough photon energy, see Appendix B). Astrophysical examples of this type of line broadening include emission lines in Wolf-Rayet stars (Münch 1950; Castor et al. 1970; Hillier 1984), absorption lines in O and B stars (Hummer & Mihalas 1967), emission lines from AGN (Kaneko & Ohtani 1968; Weymann 1970; Kallman & Krolik 1986; Laor 2006), Fe K α emission in x-ray binaries (Ross 1979; George & Fabian 1991), and some type II supernovae (Chugai 2001; Dessart et al. 2009; Gal-Yam et al. 2014).

When scattering-broadening dominates in a plasma of moderate electron scattering optical depth τ_e , the result is narrow line core consisting of un-scattered photons, surrounded by a broad component referred to as the “wings” or “pedestal.” These wings have the potential to be misinterpreted as kinematic broadening, leading to overestimates of bulk velocities (e.g. Chugai 2001; Dessart et al. 2009). A similar issue may arise in the interpretation of P-Cygni profiles when τ_e is non-negligible (Auer & van Blerkom 1972).

Here we present radiative transfer calculations that include the physics of non-coherent electron scattering as described in Appendix B. We use the same gas density profile as described in the previous section. We do not attempt to model the continuum emission, but rather consider only line emission coming from $r_{\text{in}} = 10^{14} \text{ cm}$

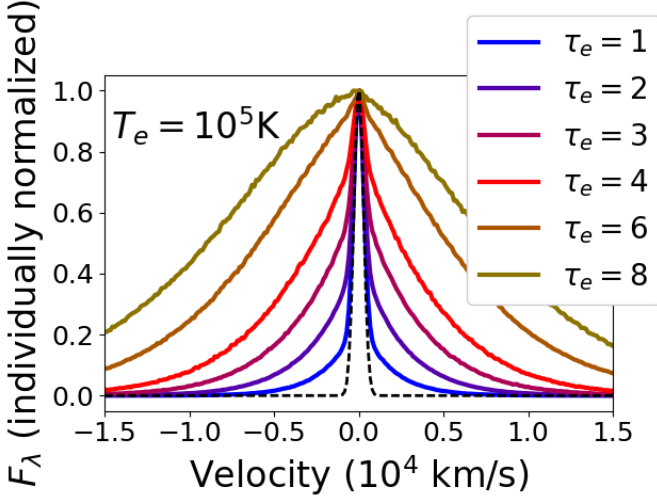


Figure 3. Demonstration of the line-broadening effect of non-coherent electron scattering. The plot shows model line profiles for varying values of electron scattering optical depth τ_e in a gas with no net velocity and $T_e = 10^5$ K throughout. All fluxes have been scaled to their value at line center. The characteristic core and wing profile is visible at lower values of τ_e . As τ_e increases, the wings become wider and the core contribution becomes smaller, and at sufficiently high τ_e the line appears broad without a distinguishable core.

that then scatters on its way out to the observer. For simplicity, we set the electron temperature $T_e(r)$ to a constant value of 10^5 K.

Figure 3 shows the resulting continuum-subtracted line profiles for different values of τ_e , the integrated electron scattering optical depth through the envelope. For $\tau_e \lesssim 5$, the characteristic core-and-wing profile is visible, with a larger portion of the core escaping at lower optical depth (c.f. Chugai 2001). The narrow core is composed primarily of line photons that have traveled all the way through the envelope without scattering. The wings are built up from photons that have diffused in frequency space as a result of multiple Doppler shifts from multiple electron scatterings. For larger optical depths ($\tau_e \gtrsim 5$) only the wings are visible.

We compare these scatter-broadened line models to the host-subtracted spectra of the TDE ASASSN-14li (Holoien et al. 2016b), for which we have subtracted a linear fit to the continuum near $H\alpha$. Model fits for two epochs are shown in Figure 4 and Figure 5. The value of τ_e was the single parameter that was changed to produce the two fits, with $\tau_e = 3.3$ for the early spectrum and $\tau_e = 2.0$ for the later spectrum.

In Figure 6 we let T_e follow an $r^{-3/4}$ relation, which corresponds to the diffusion approximation for the radiative energy density e_{rad} given our r^{-2} density profile, with the added assumption that $T_e = (e_{\text{rad}}/a_{\text{rad}})^{1/4}$. This results in a temperature of 1.8×10^4 K at the outer radius $R = 10^{15}$ cm. This temperature approximates the electron temperatures we expect at sufficient depth

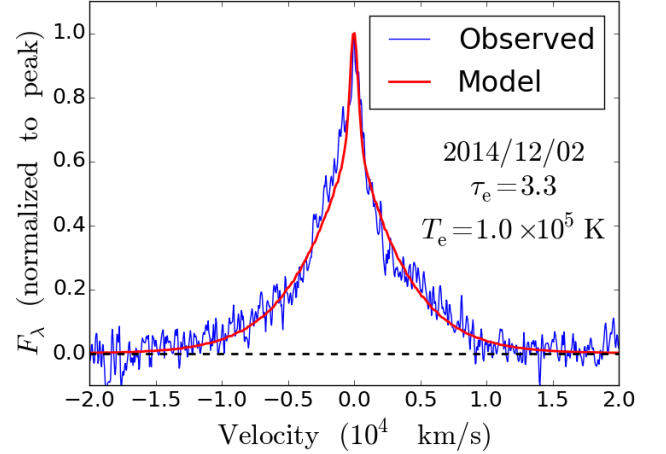


Figure 4. A model fit to the host-subtracted and continuum-subtracted $H\alpha$ line profile of ASASSN-14li taken 9 days after discovery (Holoien et al. 2016b).

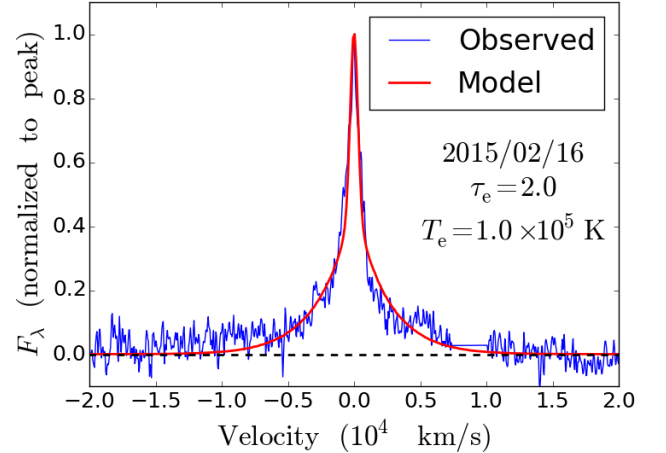


Figure 5. The same as Figure 4, but for the spectrum taken 85 days after discovery. By simply adjusting the value of τ_e in the model, a new fit has been obtained.

in the full problem. In the figure we see that a fit of similar quality as before is obtained, with τ_e adjusted upward to 3.8.

The high quality of the model fits to the line profiles of ASASSN-14li suggest that non-coherent electron scattering may have had a dominant effect in setting the line widths for this TDE. This would imply that the evolution of the line widths reflects a reduction in optical depth over time, rather than any kinematic behavior. The fitted values of τ_e , however, should be considered lower bounds, because in the model the line photons were emitted at a constant radius. In order to obtain a similar line width in the more realistic case when photons are emitted at a range of radii, including close to the photosphere, a higher optical depth will be required.

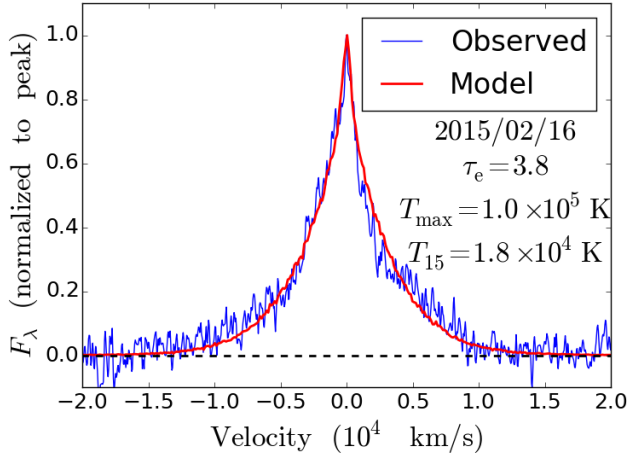


Figure 6. The same as Figure 4, but now the model includes an electron temperature gradient in accordance with radiative diffusion. The best-fit value of τ_e is adjusted upwards to 3.8 instead of 3.3 as was found in Figure 4.

5. CALCULATIONS COMBINING OUTFLOWS AND ELECTRON SCATTERING

In the previous sections, we used simplified setups to illustrate how outflows, the line source function, and non-coherent electron scattering (NCES) affect the line profiles. We now present more realistic calculations of line formation in TDE outflows that include NCES and with the line source function and opacity derived from a more detailed NLTE analysis, which includes the effect of adiabatic reprocessing of the continuum (see Appendix A for details). The procedure we use can be applied to any line, but for concreteness we use H α .

5.1. Homologous expansion at different maximum velocities

Figure 7 shows our more detailed line profile calculations for homologous outflow models with various values of v_{sc} . The gas density and extent are set using the fiducial values introduced in Section 3. We set T_{in} , the gas temperature at r_{in} , equal to 2.93×10^5 K, chosen so that the diffusive luminosity of the fiducial envelope with $v_{sc} = 10^4$ km s $^{-1}$ is 10^{45} erg s $^{-1}$. The continuum thermalization depth resides at $r_{th} = 2.7 \times 10^{14}$ cm.

The first thing to note is that the lines are primarily in emission. There is no blueshifted absorption trough as seen in the P-Cygni profiles associated with homologous outflow in a supernova. As explained in Section 3 this is due to the high line source function found for lines in TDE outflows. The peak of the model line profile is also blueshifted, with a higher value of v_{sc} producing a larger blueshift. The lines are also asymmetric, with an extended red wing.

Before proceeding to show more results, we will explain what causes these line shapes. We have already

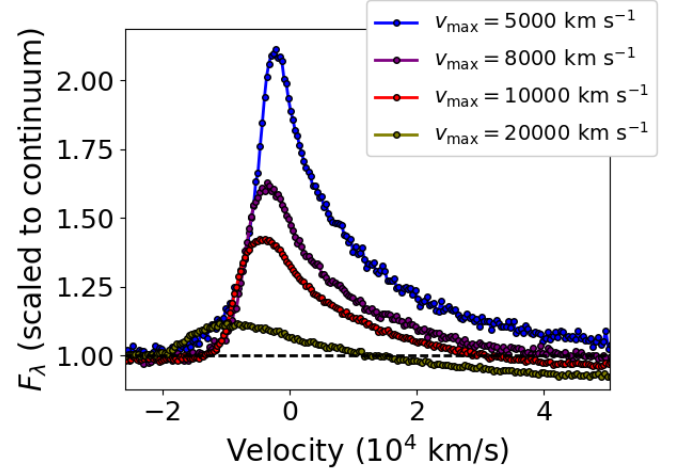


Figure 7. Computed H α line profiles for a homologously expanding outflow with various values of v_{sc} . The continuum fluxes are, from lowest to highest v_{sc} , 1.3 , 2.0 , 2.6 , and 6.5×10^{38} erg s $^{-1}$ Å $^{-1}$. For all lines in this figure, the continuum photosphere r_{th} is located at 2.7×10^{14} cm, and the outer radius $R = 10^{15}$ cm.

seen that for a sufficiently high line excitation temperature T_{ex} , lines that form in an expanding atmosphere appear purely in emission. We also saw that in the absence of electron scattering, the lines possess a shoulder at Doppler velocity of the continuum photosphere, v_{th} . The inclusion of electron scattering smooths the shoulder into a blueshifted peak. Finally, the red tail of line emission arises because the photons are scattering in an expanding flow. Just as the continuum radiation is redshifted adiabatically in an outflow, a similar effect is seen on the line photons.

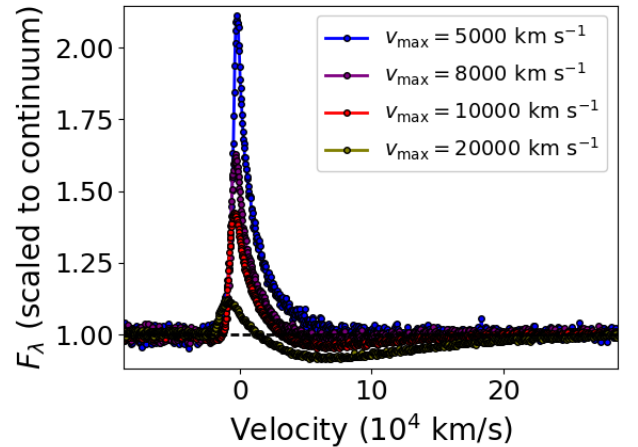


Figure 8. The same as Figure 7, but displayed over a wider range of wavelengths (Doppler velocities). At higher v_{sc} , a redshifted absorption trough appears.

Figure 8 shows the same model spectra as Figure 7,

but zoomed out over a larger range of wavelengths. At higher v_{sc} , a *redshifted* absorption trough is visible, although for our setup it is not very prominent for v_{sc} less than 10^4 km s^{-1} and would be difficult to detect given the signal-to-noise limitations in most spectra.

These line profiles bear a resemblance to the inverse P-Cygni profiles that result from the so-called “top-lighting” effect from ISM interaction in a supernova (Branch et al. 2000), but they arise here for different reasons. In the case of (Branch et al. 2000), the non-shell emission at each wavelength arises from constant projected velocity surfaces, which is not the case here because of the high τ_e . In our case, the redshifted absorption is related to the overall adiabatic evolution of the continuum radiation. Starting at the inner boundary and moving out, the entire continuum is being redshifted as photons do work on the expanding envelope. When continuum radiation is absorbed by the line, the adiabatic redshifting transfers the absorption feature to longer wavelengths.

5.2. Homologous expansion with different outer radii

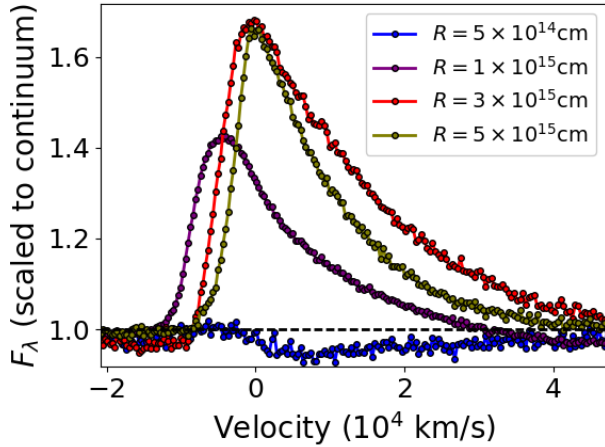


Figure 9. Computed $\text{H}\alpha$ line profiles for homologous expansion and $v_{\text{sc}} = 10^4 \text{ km s}^{-1}$, but for various values of the outer truncation radius R . This crudely represents a time sequence for a homologous outflow. The continuum fluxes are, from lowest to highest R , 7.3, 2.6, 0.91, and $0.85 \times 10^{38} \text{ erg s}^{-1} \text{ \AA}^{-1}$. The continuum thermalization photosphere r_{th} is located at 3.6, 2.7, 1.0, and $1.0 \times 10^{14} \text{ cm}$, following the procedure described in Section A.5.

Figure 9 shows the effect of varying R , while keeping v_{sc} fixed at 10^4 km s^{-1} . We keep the envelope mass fixed at $0.25 M_{\odot}$ and the diffusive luminosity fixed at $10^{45} \text{ erg s}^{-1}$ (the true bolometric luminosity will be affected by how the advective properties of the envelope change as we adjust its size). This set of calculations can be considered a crude representation of the time evolution of a TDE outflow where the radial extent of the

outflow increases with time. We caution, however, that a time-dependent radiation-hydrodynamic calculation is necessary to truly model the time evolution.

For the smallest value of R considered, $5 \times 10^{14} \text{ cm}$, the line profile becomes a shallow absorption, nearly blending into the continuum entirely. A similar effect was seen in R16 for a static envelope of otherwise similar parameters. At larger R , the emission reappears. As R increases, the peak of the line becomes more centered, and at $R = 5 \times 10^{15} \text{ cm}$, the line is entirely centered on the rest wavelength. The line also narrows and becomes more symmetric as R increases.

5.3. Constant-velocity vs homologous expansion

Figure 10 compares the line profile of a homologous expanding model with $v_{\text{sc}} = 10^4 \text{ km s}^{-1}$ to a model where the entire outflow moves with the same velocity v_{sc} . The line profiles are similar, but due to the enhanced adiabatic reprocessing in the constant-velocity case (see Section A.2 for more details), the strength of the continuum is higher at the $\text{H}\alpha$ wavelength, reducing the contrast of the line in that case.

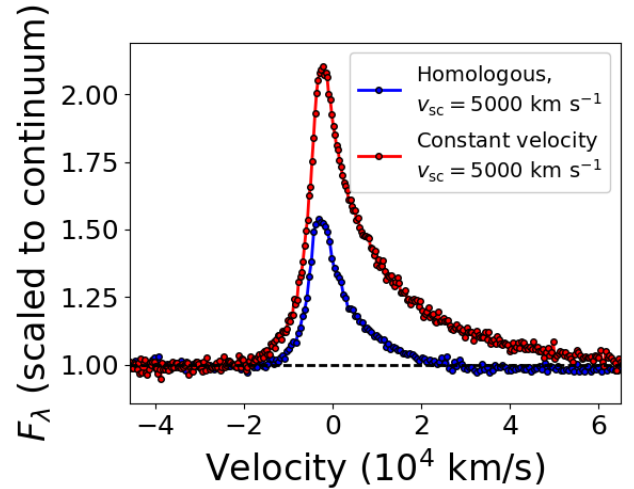


Figure 10. Computed $\text{H}\alpha$ line profiles with $v_{\text{sc}} = 10^4 \text{ km s}^{-1}$, comparing the case of homologous expansion to that of constant-velocity. The continuum flux is $1.3 \times 10^{38} \text{ erg s}^{-1} \text{ \AA}^{-1}$ for the homologous case, and $4.3 \times 10^{38} \text{ erg s}^{-1} \text{ \AA}^{-1}$ for the constant-velocity calculation. The continuum thermalization photosphere r_{th} is $2.7 \times 10^{14} \text{ cm}$ for the homologous case and $2.9 \times 10^{14} \text{ cm}$ for the constant-velocity case.

5.4. Comparison to ASASSN-14ae

Figure 11 displays how our fiducial $\text{H}\alpha$ line profile compares to the early (4 days post-discovery) line profile observed from ASASSN-14ae (Holoien et al. 2014), accessed via the Weizmann interactive supernova data repository (Yaron & Gal-Yam 2012). We succeed in obtaining a good match to the ratio of the peak line flux to

that of the continuum. We also match a number of qualitative features of the line: its blueshifted peak, overall width, and asymmetry in the form of an extended red wing. The match is not perfect, however. The asymmetry in our computed line is more pronounced than the observed one. Our line also does not extend as far to the blue as the observed one. If we were to increase v_{sc} , we would generate flux at bluer wavelengths, but at the cost of worsening all other aspects of the fit.

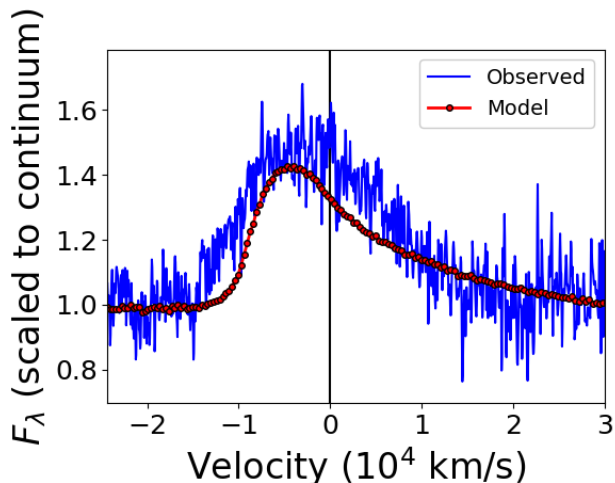


Figure 11. Comparison of the observed $H\alpha$ line profile of ASASSN-14ae (blue curve, taken 4 days post-discovery) to a radiative transfer model of a homologously outflow with $v_{sc} = 10^4 \text{ km s}^{-1}$ (red curve). The model reproduces the key features of the line profile, including the blueshifted line peak and asymmetric red wing. The model continuum flux, however, is roughly a factor of 4.5 below the observed host-subtracted value at this epoch.

There is another important way in which our model falls short. While we match the *relative* strength of the line and the continuum, the value of our continuum flux at line-center, $2.6 \times 10^{38} \text{ erg s}^{-1} \text{ \AA}^{-1}$, is about a factor of 4.5 too low compared to the observed host-subtracted value. The model was also designed to generate a bolometric luminosity of $10^{45} \text{ erg s}^{-1}$, whereas the estimated bolometric luminosity at this epoch reported in [Holoien et al. \(2014\)](#) is about an order of magnitude lower. A more thorough exploration of parameter space might produce a fit that succeeds better in matching these aspects of the observations. In particular, the observation suggests a higher envelope mass and/or absorption reprocessing efficiency than we have assumed here.

6. DISCUSSION AND CONCLUSIONS

Asymmetric emission lines with blueshifted peaks and extended red wings can be signatures of outflows in TDEs. The H and He lines will generally not possess blueshifted absorption in the manner of a P-Cygni profile, because of the high excitation temperature of the

lines. The red wing of the line is a result of the redshifting of line photons as they scatter through an expanding atmosphere. For a prompt outflow that expands with time, the initially blueshifted peak will become more centered, and the line asymmetry will decrease over time. These effects might help to explain the behavior of $H\alpha$ in ASASSN-14ae, and the behavior of the He II line in PTF-09ge, ASASSN-15oi, and PS1-10jh when the emission is more blueshifted than expected for the Bowen blend near this line.

Electron scattering can play a significant role in setting the width of the emission lines. In the absence of an outflow or un-attenuated emission from an accretion disk, it may be the dominant source of the width. The narrowing of emission lines over time, as has been observed in events including ASASSN-14li and ASASSN-14ae, might be more easily explained in terms of an evolution in the optical depth of the line-emitting region over time, rather than an evolution in its kinematics. We have tested this idea by performing fits to the ASASSN-14li $H\alpha$ line profiles, varying only τ_e and obtaining fits at two epochs. We remain agnostic at this time as to what hydrodynamic processes may cause the optical depth to drop over time. The role of electron scattering in shaping spectral features could be further tested via spectropolarimetry, as suggested by [Chugai \(2001\)](#).

Even in the presence of an outflow, a sufficiently compact reprocessing envelope can lead to the near-total suppression of the $H\alpha$ line with respect to the continuum, similar to what was found for a static envelope in R16, and relevant to TDEs such as PS1-10jh which show no detectable hydrogen emission in their spectra. However, we do see some evidence that as the outflow proceeds and the envelope expands, the strength of the hydrogen line with respect to the continuum may change.

Though the models in this paper help illuminate several key features of line formation in TDE outflows, we have made a number of assumptions and simplifications that will need to be improved upon in future work. We have assumed spherical symmetry, which prevents us from accounting for viewing angle effects. While we have accounted for radial motion of the gas in an outflow, we have not included rotational motion, which in some scenarios may be of comparable magnitude. Our treatment is time-independent in the sense that we assume the radiation diffusion time is small compared to the hydrodynamic timescales, which may not be true especially at times before the light curve peak.

To determine the gas density and velocity as a function of position and time, rather than treating these quantities parametrically as we have done here, we would need to perform radiation-hydrodynamics simulations in three spatial dimensions.

Despite these shortcomings, the trends we have described here are likely qualitatively robust and pave the way toward a more complete understanding of the optical and UV emission from TDEs.

ACKNOWLEDGMENTS

We thank Iair Arcavi, Nadia Blagorodnova, Jon S. Brown, Brad Cenko, Suvi Gezari, Tom Holoien, Julian Krolik, and Brian Metzger for helpful conversations. NR acknowledges the support of a Joint Space-Science In-

stitute prize postdoctoral fellowship. DK is supported in part by a Department of Energy Office of Nuclear Physics Early Career Award, and by the Director, Office of Energy Research, Office of High Energy and Nuclear Physics, Divisions of Nuclear Physics, of the U.S. Department of Energy under Contract No. DE-AC02-05CH11231. This work was supported in part by NSF Astronomy and Astrophysics grant 1616754. Simulations were performed on the Deepthought2 high-performance computing cluster at the University of Maryland.

APPENDIX

A. TREATMENT OF THE CONTINUUM RADIATION AND LINE SOURCE FUNCTIONS

A.1. *Scope*

In principle, as in R16, we need to simultaneously (iteratively) solve the non-LTE equations coupled with the radiative transfer equation. The former determine the emissivity and opacity of each line, while the latter determines quantities such as photoionization rates and mean radiative intensities at line wavelengths $\bar{J}_{\lambda, \text{line}}$, which enter into the non-LTE equations that determine the line emissivities and opacities.

However, for computational expediency, in this study we forgo the iterative approach. We instead solve the non-LTE equations assuming that the continuum radiation is entirely responsible for setting the line emissivities and opacities. In other words, we assume that $\bar{J}_{\lambda, \text{line}}$ is equal to the value of J_{λ} at the neighboring continuum. Given that observations indicate that the flux at line center in TDEs is generally within a factor of a few of the neighboring continuum flux (with the notable exception of ASASSN-14li), we feel that this is a reasonable approximation. To the extent that this approximation fails, as it is increasingly likely to do when applied to spectra taken at later times, it will introduce quantitative errors into our predictions for the line ratios and widths, but we should still be able to discern qualitative patterns.

We also simplify our calculation of the properties of the continuum radiation. We track two effects: 1) Adiabatic reddening of the spectrum injected at the lower boundary of the envelope, and 2) Absorption of soft x-ray and UV photons followed by emission at longer wavelengths. We describe our treatment of the first effect in Section A.2, and of the second in Section A.3. We go on to describe how we can translate these properties of the continuum radiation into line opacities and source functions in Section A.4. We provide additional details for how we use this information in our radiative transfer calculations in Section A.5.

A.2. *Radiation energy density as function of radius: role of central engine and adiabatic losses*

We consider a fluid in which radiation dominates its internal energy. We assume that the gas is dense enough that the radiation is in the diffusion regime (but not necessarily in local thermodynamic equilibrium). To order v/c (where v is the fluid velocity and c is the speed of light), and in spherical symmetry with radial coordinate r , the first law of thermodynamics for a fluid element is expressed by (Mihalas & Mihalas 1984)

$$\frac{D}{Dt} \left(\frac{E_0}{\rho} \right) + \frac{1}{3} E_0 \frac{D}{Dt} \left(\frac{1}{\rho} \right) = - \frac{1}{4\pi r^2 \rho} \frac{\partial L_0}{\partial r}, \quad (\text{A1})$$

where E_0 is the radiation energy density per unit volume as measured in the co-moving frame of the fluid, ρ is the fluid mass density, $L_0 = 4\pi r^2 F_0$, F_0 is the co-moving radiative flux, and D/Dt is the Lagrangian (material) derivative operator. We have used the fact that the radiation pressure in the diffusion regime is equal to $1/3 E_0$.

We consider a medium that is highly enough ionized such that electron scattering dominates the opacity, which we'll denote by κ_{es} , with corresponding optical depth τ_e . This opacity is evaluated in the co-moving frame of the fluid. The condition of radiative diffusion then allows us to write

$$\frac{L_0}{4\pi r^2} = - \frac{1}{3} \frac{c}{\rho \kappa_{\text{es}}} \frac{\partial E_0}{\partial r}. \quad (\text{A2})$$

We also make use of the continuity equation

$$\frac{D\rho}{Dt} = -\rho \left(\vec{\nabla} \cdot \vec{v} \right). \quad (\text{A3})$$

Combining all of these, and using spherical symmetry to expand the $\nabla \cdot \vec{v}$ terms, gives

$$\frac{\partial E_0}{\partial t} + v \frac{\partial E_0}{\partial r} + \frac{4}{3} E_0 \left(\frac{\partial v}{\partial r} + \frac{2v}{r} \right) = \frac{1}{r^2} \frac{\partial}{\partial r} \left(\frac{c}{3\rho\kappa_{\text{es}}} r^2 \frac{\partial E_0}{\partial r} \right). \quad (\text{A4})$$

At this point we will drop the 0 subscript for the radiation energy density, with the understanding that E always refers to the co-moving radiative energy density. To convert to the lab-frame value of E , we can use the relation

$$\begin{aligned} E_{\text{lab}} &= E_0 + 2 \frac{v}{c} \frac{F_0}{c} \\ &= E_0 - \frac{2v}{3\rho\kappa_{\text{es}}c} \frac{\partial E_0}{\partial r}, \end{aligned} \quad (\text{A5})$$

which is accurate to order v/c (Mihalas & Mihalas 1984), and the second equality makes use of the diffusion approximation.

Next we follow Arnett (1980) (hereafter A80) by assuming the solution for E is separable in space and time, and factoring out the adiabatic dependence on $R(t)$,

$$E(r, t) = E(r_{\text{in}}, 0) \psi(x) \phi(t) \frac{R^4(0)}{R^4(t)}, \quad (\text{A6})$$

where $x \equiv r/R(t)$. We obtain

$$R(t) \frac{\dot{\phi}}{\phi} - 4\dot{R} + v \frac{\psi'}{\psi} + \frac{4}{3} \left(v' + \frac{2v}{x} \right) = \frac{c}{3R(t)} \frac{1}{\psi x^2} \frac{\partial}{\partial x} \left(\frac{x^2}{\rho\kappa_{\text{es}}} \psi' \right), \quad (\text{A7})$$

where dots denote partial derivatives with respect to time, and primes denote partial derivatives with respect to x .

If we were to continue following A80, we would assume homologous expansion in the form $v = v_{\text{sc}}x$, and for an appropriate scale velocity v_{sc} . This leads to a cancellation of the second and fourth terms of equation (A7), resulting in

$$R(t) \frac{\dot{\phi}}{\phi} + v_{\text{sc}}x \frac{\psi'}{\psi} = \frac{c}{3R(t)} \frac{1}{\psi x^2} \frac{\partial}{\partial x} \left(\frac{x^2}{\rho\kappa_{\text{es}}} \psi' \right). \quad (\text{A8})$$

The second term of equation (A8) does not appear in A80. In our application, this term will be important, so we proceed differently. If the radiation diffusion time is small compared to the time over which the envelope properties change, then the terms containing partial time derivatives in equation (A7) are small compared to the other terms. Dropping those terms, and only those terms, we are left with

$$v\psi' + \frac{4}{3} \left(v' + \frac{2v}{x} \right) \psi = \frac{c}{3R(t)} \frac{1}{x^2} \frac{\partial}{\partial x} \left(\frac{x^2}{\rho\kappa_{\text{es}}} \psi' \right). \quad (\text{A9})$$

To proceed further we need $v(r)$ and $\rho(r)$. These are set by the hydrodynamics, particularly through the inclusion of the momentum conservation equation, and in principle we need to solve for them simultaneously. Such solutions (time-independent) have been described in Shen et al. (2016). Alternatively, we can specify guesses for these in advance. For example, we can again consider homologous expansion, so that $v = v_{\text{sc}}r/R$. We can also consider a constant-velocity case where $v = v_{\text{sc}}$ at all radii in our computational domain (i.e. the gas was initially accelerated at unresolved radii). These velocity profiles are within the range of outcomes of the Shen et al. (2016) solutions, in which $v \propto r$ at small radii and asymptotes to a constant at large radii. We'll leave ρ as a generic function of radius. We'll introduce one final non-dimensional variable $\eta \equiv \rho(x)/\rho_{\text{in}}$ where the subscript "in" refers to the value at the inner boundary. We obtain

$$\psi'' = \left(\frac{\eta'}{\eta} - \frac{2}{x} \right) \psi' + \alpha \eta (x\psi' + 4\psi) \quad (\text{homologous}) \quad (\text{A10a})$$

$$\psi'' = \left(\frac{\eta'}{\eta} - \frac{2}{x} \right) \psi' + \alpha \eta \left(\psi' + \frac{8}{3} \frac{\psi}{x} \right) \quad (\text{constant velocity}), \quad (\text{A10b})$$

where

$$\alpha \equiv 3 \frac{v_{\text{sc}}}{c} \rho_{\text{in}} \kappa_{\text{es}} R. \quad (\text{A11})$$

We see that α encodes information about both the optical depth of the envelope and the gas dynamical time.

We treat the density as a power-law, $\eta = x^{-n}$, that is truncated at radius R . The density power-law n and the value of ρ_{in} are free parameters.

Now we must specify boundary conditions. As in A80, the Eddington approximation for the outer boundary results in

$$\psi(1) = -\frac{2}{3}\psi'(1)\frac{1}{\rho(R)\kappa_{\text{es}}R} . \quad (\text{A12})$$

Finally we need to specify the flux emanating from the inner boundary by finding the appropriate value for ψ' at the inner boundary. In the supernova situation that flux is usually taken to be zero, but here we are expecting a large luminosity to coming from the TDE engine. From the diffusion equation for the radiation energy density (equation (A2)), we have

$$\psi'(x_{\text{in}}) \approx -\frac{3\rho\kappa_{\text{es}}L}{4\pi c r_{\text{in}}^2} . \quad (\text{A13})$$

However, to find the exact value of the inner flux, we must solve the two-point boundary value problem. We proceed via the shooting technique. We start at the outer boundary, with a guess for $\psi(1)$. We use the outer boundary condition (A12) to find ψ' there. Next we solve equation (A10), moving to smaller radii until we reach the inner boundary. By definition,

$$\psi(x_{\text{in}}) = 1 , \quad (\text{A14})$$

so we adjust our guess for $\psi(x_{\text{out}})$ until this is achieved. In so doing we find the appropriate value of not only $\psi(1)$, but also of ψ' at the inner boundary.

While the solution described above sets the ratio between ψ at the inner and outer boundaries, the physical value of the radiation energy density at the inner boundary, E_{in} , remains a free parameter. Additional free parameters are the physical values for r_{in} and R . At the inner boundary, the radiation spectrum is a blackbody with temperature T_{in} where $E_{\text{in}} = a_{\text{rad}}T_{\text{in}}^4$.

Figure A1 shows solutions for $\psi(x)$ for three different guesses for the velocity structure. The other parameters, taken to be the same for all three curves, are $r_{\text{in}} = 10^{14}$ cm, $R = 10^{15}$ cm, $v_{\text{sc}} = 10^4$ km s $^{-1}$, density power $n = 2$, and $\rho_{\text{in}} = 4.32 \times 10^{-12}$ g cm $^{-3}$, which together with the other parameters implies an envelope mass of $0.25 M_{\odot}$. The electron scattering opacity κ_{es} is set for a fully ionized envelope consisting of hydrogen and helium at a solar abundance ratio, which evaluates to 0.34 cm 2 g $^{-1}$. This results in an electron scattering optical depth $\tau_e = 137$. The resulting value of α is 152 for the homologous and constant-velocity envelopes.

To better understand Figure A1, we can track how the components of the luminosity vary with radius in these models. Through each spherical shell of the envelope, there will be a flux of both advected radiative luminosity and diffusing radiative luminosity. There will also be a portion of the radiative energy that is lost to adiabatic work on the gas. The sum of these three components should be constant at each position. Explicitly, these luminosity components are

$$\begin{aligned} L_{\text{diff}} &= -4\pi r^2 \frac{c}{3\rho\kappa_{\text{es}}} \frac{dE}{dr} \\ L_{\text{adv}} &= 4\pi r^2 v E \\ dW_{\text{adb}}/dt &= \int p_{\text{rad}} (\vec{\nabla} \cdot \vec{v}) dV \\ &= \int 4\pi r^2 \frac{1}{3} E \left(\frac{\partial v}{\partial r} + \frac{2v}{r} \right) dr . \end{aligned} \quad (\text{A15})$$

Figure A2 shows the luminosity components for the envelope described above undergoing homologous expansion, and for a constant-velocity envelope. The analogous plot for the static envelope would show the orange curve overlapping with the black curve, with the green and blue curves at zero.

In both figures, nearly all of the radiative transfer at the outer boundary is diffusive. For the constant-velocity envelope, the energy transfer at small radii is primarily advective, while diffusion takes over at about $x = 0.5$. This corresponds to what is termed the “trapping radius” in the accretion literature (Begelman 1979; Meier 1982) and to the radiation breakout radius in the supernova literature (Chevalier 1992), where the radiation diffusion time through the remaining envelope becomes comparable to the gas dynamical time r/v . For our setup, no trapping radius exists for the homologous case, as diffusion dominates the energy transfer at all radii.

The total radiative luminosity represented by the flat black curve does not correspond to the same value in the two figures. These calculations were set up to have the same radiative energy density at the inner boundary. The flux at the inner boundary adjusts as a result of the solution of the two-point boundary value problem such that it is larger

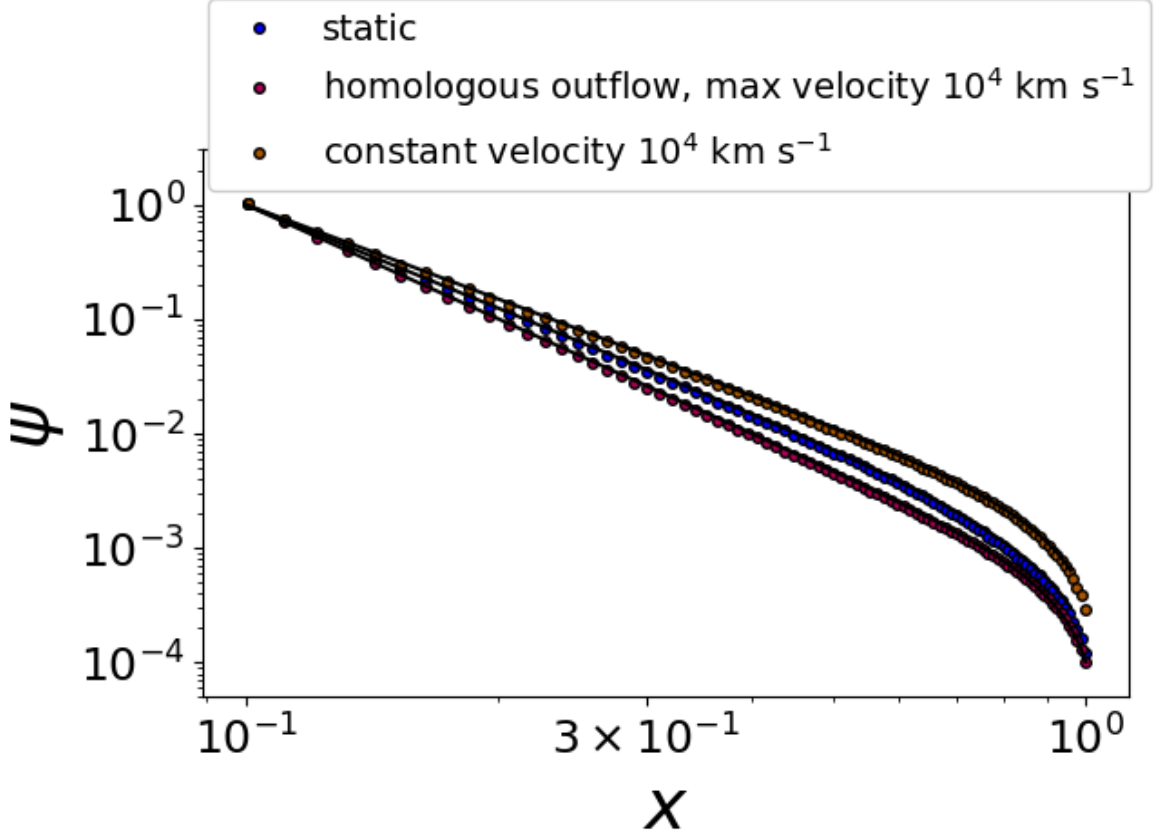


Figure A1. Nondimensional radiation energy density ψ as a function of nondimensional radius x . Circle markers are output from Monte Carlo radiative transfer calculation divided into 1024 radial zones, with data from every twelfth zone plotted. The solid black lines are solutions to the ordinary differential equation (A10) subject to the boundary conditions from equations (A12) and (A14). These solutions assume that the radiation diffusion time is small compared to the time over which the envelope properties change. The maximum velocity for the homologously expanding envelope is 10^4 km s^{-1} , which is also the velocity used for the constant-velocity envelope, and both these envelopes have $\alpha = 152$.

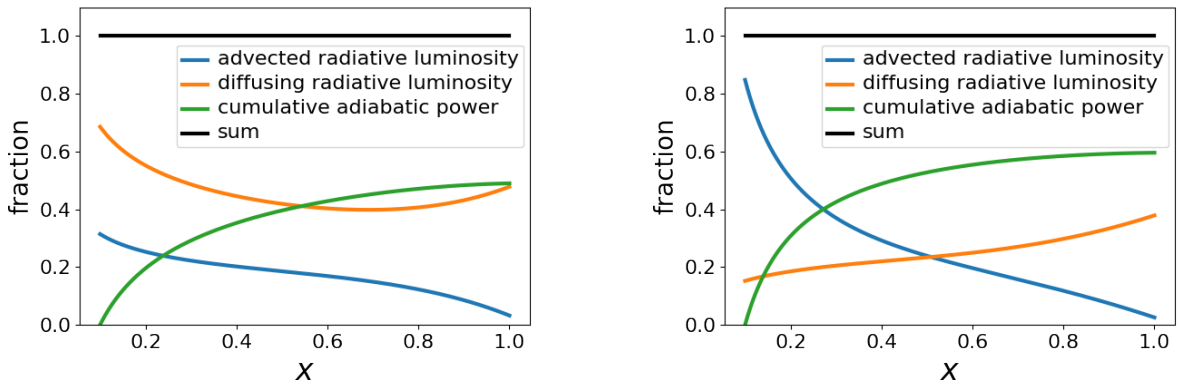


Figure A2. The components of luminosity as a function of radius, for (left) a velocity profile corresponding to homologous expansion and (right) a constant-velocity outflow.

for the constant-velocity case than the homologous expansion case. This is a consequence of the large advective flux of radiative energy at the inner boundary of the constant-velocity calculation. This helps to explain why the radiative energy density in Figure A1 is highest for the constant-velocity case, even when accounting for radiative energy loss to adiabatic expansion. Meanwhile, for the homologous case, where the advective flux at the inner boundary is much lower, the adiabatic losses result in a lower radiative energy density than for the static case.

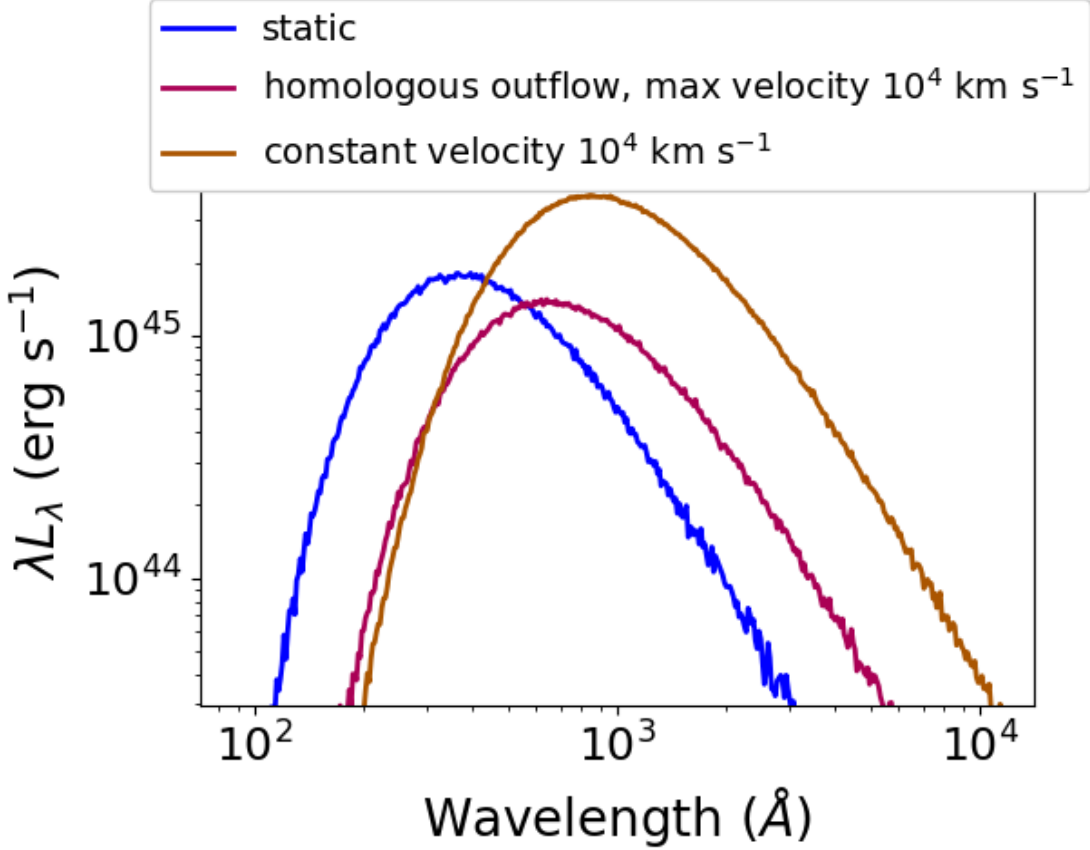


Figure A3. The effect of adiabatic reprocessing on the escaping SED for the three velocity structures considered. In all three cases, a blackbody with temperature of approximately 2.93×10^5 K was injected at the inner boundary, which for the envelope density profile corresponds to a diffusive luminosity of 10^{45} erg s $^{-1}$ at the outer boundary for the homologous atmosphere. Expanding atmospheres lead to a redshift of the injected SED, and also influence the total luminosity that escapes. The radiation energy density at the inner boundary is set to be the same in all three cases, but this means that the inner luminosity in all three cases is different.

We can use the information displayed in Figure A2 to understand how the spectrum of the radiation evolves as a function of position. The energy lost to adiabatic expansion leads to a redshifting of the spectrum. We can see this in the emergent SEDs of the three models, displayed in Figure A3. The SED peaks at longer wavelengths for the homologous and constant-velocity calculations than for the static calculation. We see that adiabatic reprocessing can make a substantial contribution to the flux that escapes at optical wavelengths, as has been discussed in past work (Strubbe & Quataert 2009; Lodato & Rossi 2011; Metzger & Stone 2016).

A.3. A simplified “two-temperature” reprocessing scheme

In R16 we demonstrated how a TDE envelope can absorb soft x-ray and UV radiation emitted from accretion onto the black hole (BH) and reprocess this to longer wavelengths. The optical continuum is ultimately composed of a blend of emission from different temperatures originating from different radii within the envelope, and its strength depends on details of the envelope structure such as its density and radial extent. Here we will collapse all of these details into an approximation formula that depends on two parameters. The first parameter is ϵ_{abs} , which acts as an average ratio of absorption opacity to electron scattering opacity for UV and soft x-ray photons. The second parameter, f , denotes the fractional temperature of the reprocessed radiation compared to T_{in} .

Consider again the effects of adiabatic expansion, as described in the previous section. The spectrum at the inner boundary is a blackbody, $B(\lambda, T_{\text{in}})$. At larger radii, the spectrum is given by

$$J_{\lambda}(r) = J(r) B[d(r)\lambda, T_{\text{in}}] , \quad (\text{A16})$$

where $d(r)$ is the photon degradation factor, defined as the mean photon energy at that radius divided by its energy at the inner boundary. In other words, $d(r) = 1 - w_{\text{ad}}(r)$, where w_{ad} is the fraction of luminosity lost to adiabatic work, as displayed by the red curves in Figure A2. The normalization factor $J(r)$ out front ensures that the wavelength-

integrated radiation energy density as a function of radius matches what we found in Section A.2, as displayed in Figure A1. We now incorporate the effect of UV/x-ray absorption and re-emission at longer wavelengths as follows:

$$J'_\lambda(r) = J(r)(B[d(r)\lambda, T_{\text{in}}]e^{-\sqrt{\epsilon_{\text{abs}}}\tau_e} + f^{-4}B[d(r)\lambda, fT_{\text{in}}](1 - e^{-\sqrt{\epsilon_{\text{abs}}}\tau_e})) . \quad (\text{A17})$$

For this single equation, τ_e is integrated from the inner boundary out. For all the calculations in this paper we will set $\epsilon_{\text{abs}} = 10^{-5}$ and $f = 1/2$. These values are informed by the full non-LTE calculations of R16. In reality, these reprocessing parameters will depend on the other parameters such as R , ρ_{in} , etc, but we choose not to account for this added complication at this time.

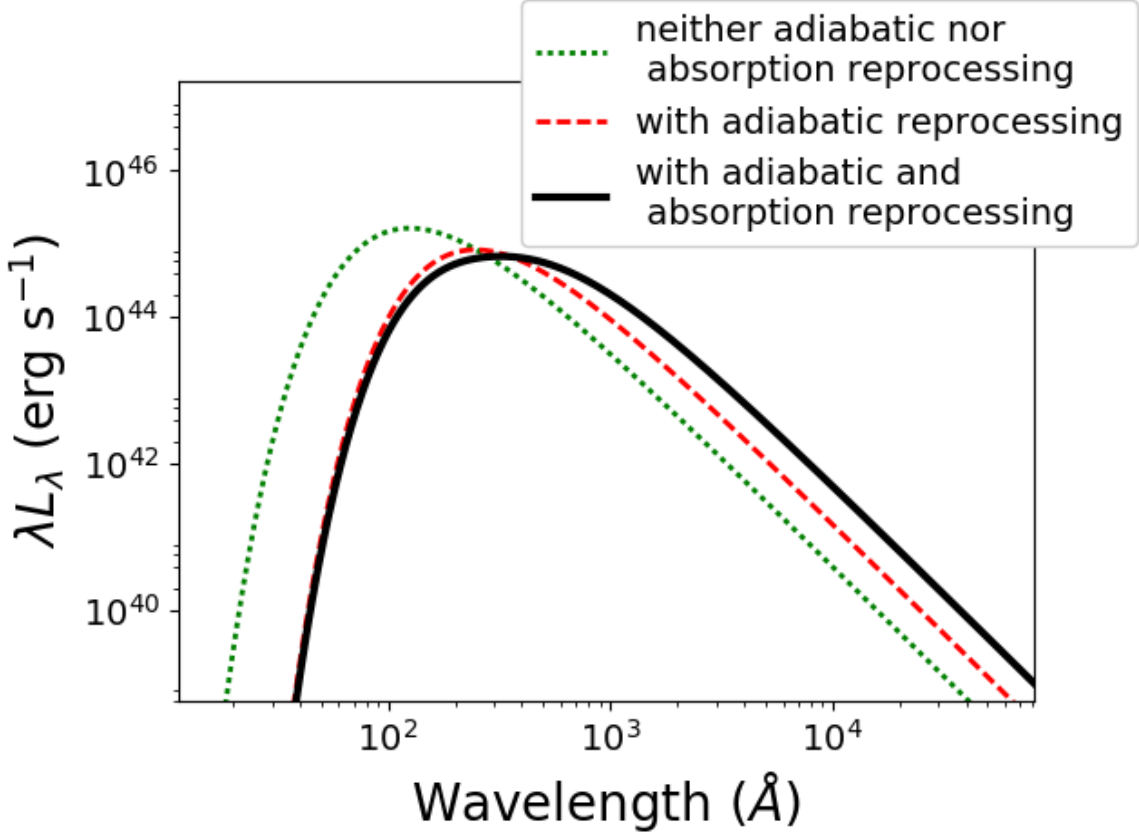


Figure A4. Spectral energy distributions from our simplified continuum reprocessing approach. The dotted green curve shows the thermal emission for $T = 2.93 \times 10^5$ K, corresponding to the static atmosphere model of Section A.2. The dashed red curve shows the SED when the adiabatic losses and advective effects are included from a homologous outflow with $v_{\text{sc}} = 10^4$ km s $^{-1}$. The solid black curve is the result of applying the “two-temperature” absorption and re-emission model described in Section A.3.

Figure A4 shows spectral energy distributions (SEDs) which summarize the results of our simplified continuum reprocessing model described in this and the previous section. For the results presented in the rest of the paper, we will incorporate the adiabatic and advective effects of an expanding atmosphere along with the “two-temperature” absorption and re-emission model, unless we state otherwise.

A.4. NLTE solution

From equation (A17), we have an approximate formula for the continuum radiation field at every radius. We can now use this to compute photoionization rates and line fluxes $\bar{J}_{\lambda, \text{line}}$, and solve the non-LTE equations assuming statistical equilibrium. We track transitions for H up to principal quantum number 6, and for He II up to principal quantum number 9. We do not include any other elements in the NLTE solution. We obtain the ionization state and bound-electron level populations for H and He at each radius, which we turn into line opacities and emissivities.

Figure A5 summarizes the entire calculation process up this point (Sections A.2 through A.4), reviewing how the envelope input parameters are turned into line emissivities and opacities for the final radiative transfer calculation from which we find the final line profile.

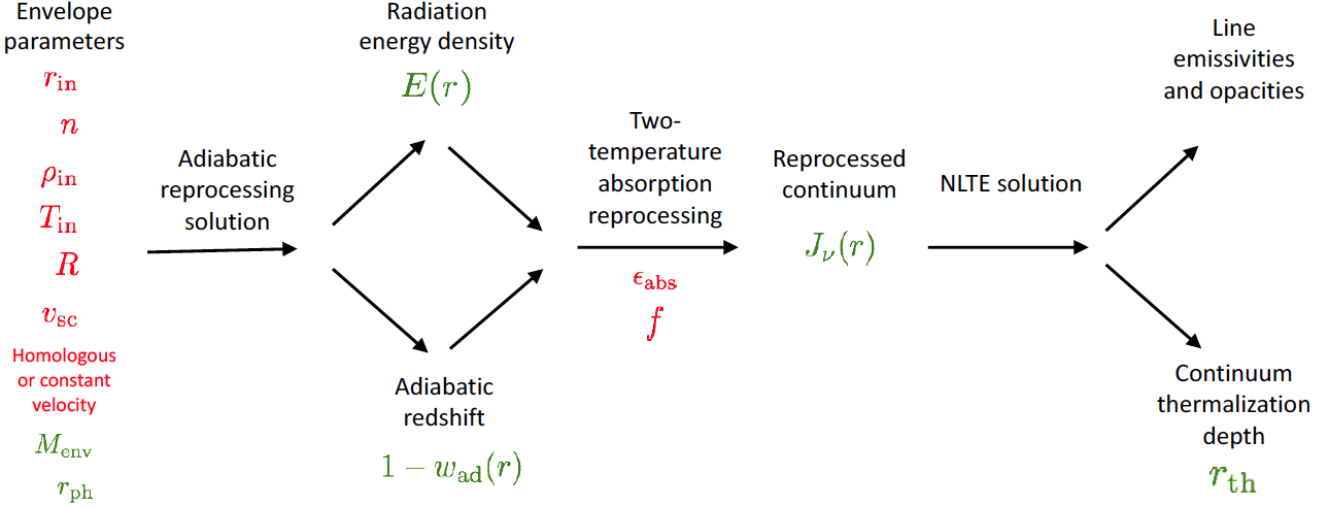


Figure A5. Flowchart illustrating the calculation stages needed to turn the input parameters into the final line emissivities and opacities. Input parameters are in red text. Derived values are in green. There are seven envelope parameters, mainly covering uncertainty in the details of the hydrodynamics. These parameters might also be connected to the BH mass, stellar mass, stellar structure, etc, and are also functions of time. We assume solar abundance ratio of H to He throughout. The two reprocessing parameters, ϵ_{abs} and f , are in principle related to the non-LTE solution and would require an iterative procedure to find self-consistently, but we simplify this process by choosing values for them initially.

A.5. Using the NLTE results in radiative transfer calculations

In the final radiative transfer calculations we make use of the tabulated line opacities and emissivities described in Section A.4, which set the rate at which photons are emitted and absorbed throughout the calculation volume.

To determine the electron temperature T_e as a function of position, we use $T_e = (E_{\text{rad}}/a_{\text{rad}})^{1/4}$, where a_{rad} is the radiation constant, and E_{rad} is the radiation energy density solution described in Section A.2. In reality T_e is set by radiative equilibrium, accounting for the heating and cooling processes of the electrons, as was done in R16. The result is that, compared to R16, we tend to under-estimate the electron temperature near the surface of the envelope. On the other hand, R16 did not include the full range of metals that can contribute to electron cooling, which if included would raise the opacity of the gas and allow it to reach a value closer to the one given by the integrated radiation energy density that we are using in this paper.

We adjust the inner photosphere r_{th} to correspond to the thermalization depth of the continuum at the line-center wavelength. To calculate the thermalization depth, we assume that free-free processes are dominating the continuum emission. In more detail, we define r_{th} as the radius corresponding to $\tau_e = 1/(\sqrt{3}\epsilon_{\text{ff}})$, where ϵ_{ff} is the ratio of the free-free opacity to the electron scattering opacity, and we evaluate these opacities based on the density and temperature at the outer edge of the envelope. As we adjust parameters, if we encounter a situation where r_{th} would fall within r_{in} , we use r_{in} as the inner boundary.

B. TREATMENT OF NON-COHERENT (COMPTON) SCATTERING

The non-coherence of electron scattering is a combination of three effects: 1) Doppler shifts introduced when boosting between the observer's frame and the initial rest-frame of the electron 2) The post-scattering recoil of the electron as measured in its initial rest frame and 3) the requirement for the photon phase space density to obey Bose-Einstein statistics. Ignoring spatial dependencies, in the limit of many scatterings, and for small enough electron temperatures such that the electrons are non-relativistic, the evolution of the photon phase-space density can be written in the form of a Fokker-Planck equation commonly known as the Kompaneets equation (Kompaneets 1957). For photon frequency ν and radiation spectral energy density u_{ν} , when $u_{\nu}c^3/(8\pi h\nu^3) \ll 1$ the third effect and its corresponding terms may be neglected. This is the case in many astrophysical applications including the present one.

The Kompaneets equation begins to lose accuracy at optical depths of order unity, and to account for spatial and temporal variation it must be combined with the radiative transfer equation. Several highly accurate numerical techniques have been developed to accomplish this (e.g. Rybicki & Hummer 1994). Here we use a Monte Carlo treatment of the scattering process. Such an approach has been used for this particular problem many times in the past, starting with Auer & van Blerkom (1972) and notably by Pozdnyakov et al. (1983).

We account for Doppler shifts due to fluid motion by first performing Lorentz transformations to boost into the co-moving frame of the fluid. We similarly account for thermal motion of the electrons by randomly sampling a velocity from a Maxwell-Boltzmann distribution, following the procedure described in Pozdnyakov et al. (1983), and then boosting into the electron rest frame. We then sample the outgoing photon direction from the classical Thomson differential scattering cross section (the Rayleigh phase function). While straightforward to include, we have omitted Klein-Nishina corrections to the total and differential cross sections, which are negligible for the photon energies of interest to us ($h\nu \ll m_e c^2$). We account for the change in photon energy due to electron recoil. Finally, we apply the inverse Lorentz transformations to move back to the co-moving frame of the fluid and then back to the lab frame.

We have validated our scattering implementation by performing a one-zone test problem similar to that described in Castor (2004) (see also Ryan et al. 2015), which tests how well we capture both effects 1 and 2 listed above. An initially monochromatic collection of photons interact with a population of thermal electrons solely via scattering. We initialize the electrons at temperature T_e , density n_e , and zero bulk velocity. We inject photons at initial frequency ν_0 , which we nondimensionalize to x_0 where $x_0 = h\nu_0/k_B T_e$, and with a total radiative energy density u_{rad} that is small compared to that of the integrated electron kinetic energy, so that T_e will remain approximately constant over the duration of the calculation. As the photons scatter, their energy distribution evolves on a timescale t_c given by

$$t_c = n_e \sigma_T c \frac{4k_B T_e}{m_e c^2} \quad (\text{B18})$$

In the absence of stimulated scattering, the photon energy spectrum should converge to a Wien distribution with mean intensity $J_{\nu, \text{final}}$ given by

$$J_{\nu, \text{final}} = \frac{2h\nu^3}{c^2} \exp \left[- \left(\frac{h\nu}{k_B T_e} + \mu \right) \right] \quad (\text{B19})$$

where μ is the chemical potential. Applying conservation of photon number, we find

$$\mu = -\ln \left[\frac{1}{2} \left(\frac{h}{k_B T_e} \right)^3 \frac{u_{\text{rad}} c^3}{8\pi h\nu_0} \right] \quad (\text{B20})$$

The results of such a test with $T_e = 10^6$ K, $n_e = 10^{12} \text{ cm}^{-3}$, $x_0 = 0.01$, and $u_{\text{rad}} = 10^{-6} a_{\text{rad}} T_e^4$ are shown in Figure B6.

REFERENCES

- Alexander, K. D., Berger, E., Guillochon, J., Zauderer, B. A., & Williams, P. K. G. 2015, ArXiv e-prints
- Alexander, K. D., Wieringa, M. H., Berger, E., Saxton, R. D., & Komossa, S. 2017, ApJ, 837, 153
- Arcavi, I., Gal-Yam, A., Sullivan, M., et al. 2014, ApJ, 793, 38
- Arnett, W. D. 1980, ApJ, 237, 541
- Auer, L. H., & van Blerkom, D. 1972, ApJ, 178, 175
- Begelman, M. C. 1979, MNRAS, 187, 237
- Blagorodnova, N., Gezari, S., Hung, T., et al. 2017, ArXiv e-prints
- Bogdanović, T., Eracleous, M., Mahadevan, S., Sigurdsson, S., & Laguna, P. 2004, ApJ, 610, 707
- Bonnerot, C., Rossi, E. M., & Lodato, G. 2017, MNRAS, 464, 2816
- Branch, D., Jeffery, D. J., Blaylock, M., & Hatano, K. 2000, PASP, 112, 217
- Brown, J. S., Kochanek, C. S., Holoien, T. W.-S., et al. 2017, ArXiv e-prints
- Castor, J. I. 2004, Radiation Hydrodynamics (Cambridge University Press)
- Castor, J. I., Smith, L. F., & van Blerkom, D. 1970, ApJ, 159, 1119
- Chandrasekhar, S. 1950, Radiative transfer. (Clarendon Press)
- Chevalier, R. A. 1992, ApJ, 394, 599
- Chornock, R., Berger, E., Gezari, S., et al. 2014, ApJ, 780, 44
- Chugai, N. N. 2001, MNRAS, 326, 1448
- Dessart, L., Hillier, D. J., Gezari, S., Basa, S., & Matheson, T. 2009, MNRAS, 394, 21
- Dirac, P. A. M. 1925, MNRAS, 85, 825
- Dong, S., Shappee, B. J., Prieto, J. L., et al. 2015, ArXiv e-prints
- Gal-Yam, A., Arcavi, I., Ofek, E. O., et al. 2014, Nature, 509, 471
- Gaskell, C. M., & Rojas Lobos, P. A. 2014, MNRAS, 438, L36
- George, I. M., & Fabian, A. C. 1991, MNRAS, 249, 352
- Gezari, S., Chornock, R., Lawrence, A., et al. 2015, ApJL, 815, L5
- Gezari, S., Chornock, R., Rest, A., et al. 2012, Nature, 485, 217
- Guillochon, J., Manukian, H., & Ramirez-Ruiz, E. 2014, ApJ, 783, 23
- Hillier, D. J. 1984, ApJ, 280, 744

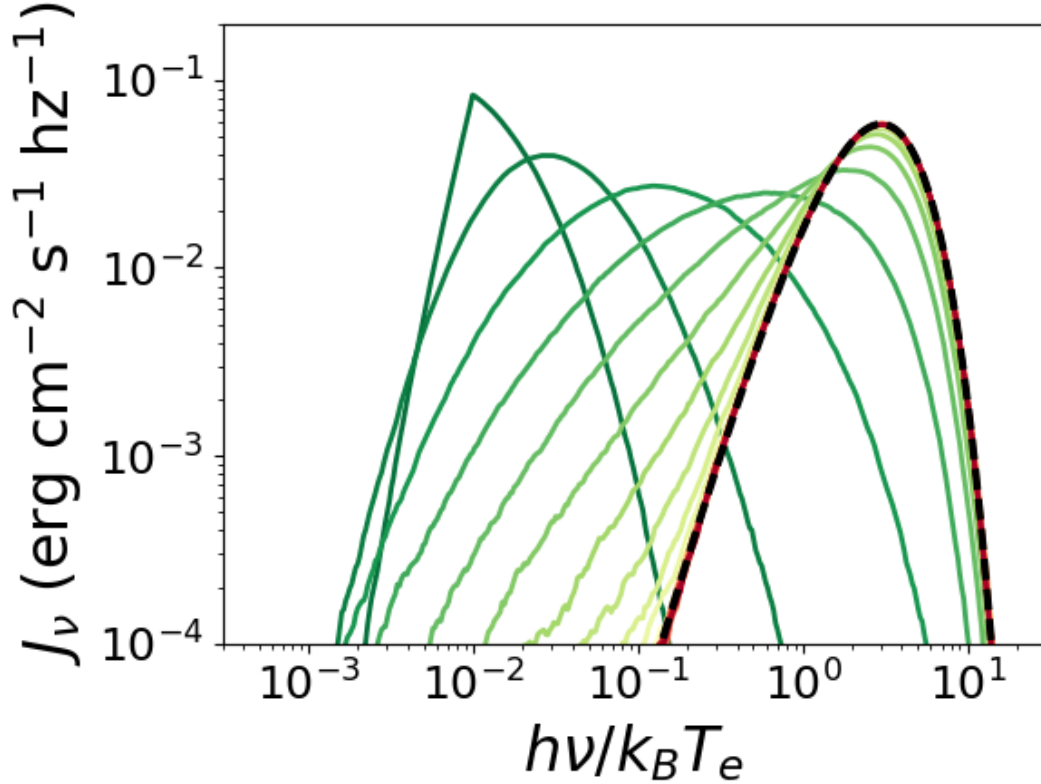


Figure B6. A test of the Comptonization physics implemented in the Monte Carlo radiative transfer. An initially monochromatic collection of photons interact with a bath of thermal electrons solely via scattering. The photon energy distribution converges to a Wien distribution (dashed black line) at a rate governed by the initial temperature of the electrons and the number of scatterings undergone by the photons. The curves are separated by times of $2t_c$. The parameter values are $T_e = 10^6$ K, $n_e = 10^{12} \text{ cm}^{-3}$, $x_0 = 0.01$, and $u_{\text{rad}} = 10^{-6} a_{\text{rad}} T_e^4$.

- Holoien, T. W.-S., Prieto, J. L., Bersier, D., et al. 2014, MNRAS, 445, 3263
- Holoien, T. W.-S., Kochanek, C. S., Prieto, J. L., et al. 2016a, MNRAS, 463, 3813
- . 2016b, MNRAS, 455, 2918
- Hummer, D. G., & Mihalas, D. 1967, ApJL, 150, L57
- Hung, T., Gezari, S., Blagorodnova, N., et al. 2017, ArXiv e-prints
- Jefferies, J. T., & Thomas, R. N. 1958, ApJ, 127, 667
- Jeffery, D. J., & Branch, D. 1990, Jerusalem Winter School for Theoretical Physics
- Jiang, Y.-F., Guillochon, J., & Loeb, A. 2016, ApJ, 830, 125
- Kallman, T. R., & Krolik, J. H. 1986, ApJ, 308, 805
- Kaneko, N., & Ohtani, H. 1968, AJ, 73, 899
- Kasen, D., Thomas, R. C., & Nugent, P. 2006, ApJ, 651, 366
- Kochanek, C. S. 1994, ApJ, 422, 508
- Kompaneets, A. 1957, Sov. Phys., JETP, 4, 730
- Krolik, J., Piran, T., Svirski, G., & Cheng, R. M. 2016, ApJ, 827, 127
- Laor, A. 2006, ApJ, 643, 112
- Leloudas, G., Fraser, M., Stone, N. C., et al. 2016, Nature Astronomy, 1, 0002
- Lodato, G., & Rossi, E. M. 2011, MNRAS, 410, 359
- Loeb, A., & Ulmer, A. 1997, ApJ, 489, 573
- Margutti, R., Metzger, B. D., Chornock, R., et al. 2016, ArXiv e-prints
- Meier, D. L. 1982, ApJ, 256, 681
- Metzger, B. D., & Stone, N. C. 2016, MNRAS, 461, 948
- Mihalas, D., & Mihalas, B. W. 1984, Foundations of radiation hydrodynamics (Oxford University Press)
- Miller, M. C. 2015, ApJ, 805, 83
- Münch, G. 1948, ApJ, 108, 116
- . 1950, ApJ, 112, 266
- Piran, T., Svirski, G., Krolik, J., Cheng, R. M., & Shiokawa, H. 2015, ApJ, 806, 164
- Pozdnyakov, L. A., Sobol, I. M., & Syunyaev, R. A. 1983, Astrophysics and Space Physics Reviews, 2, 189
- Ross, R. R. 1979, ApJ, 233, 334
- Roth, N., & Kasen, D. 2015, ApJS, 217, 9
- Roth, N., Kasen, D., Guillochon, J., & Ramirez-Ruiz, E. 2016, ApJ, 827, 3
- Ryan, B. R., Dolence, J. C., & Gammie, C. F. 2015, ApJ, 807, 31
- Rybicki, G. B., & Hummer, D. G. 1994, A&A, 290, 553
- Shen, R.-F., Nakar, E., & Piran, T. 2016, MNRAS, 459, 171
- Sobolev, V. V. 1947, Moving Envelopes of Stars [in Russian] (Leningr. Gos. Univ.)
- Strubbe, L. E., & Murray, N. 2015, MNRAS, 454, 2321
- Strubbe, L. E., & Quataert, E. 2009, MNRAS, 400, 2070
- van Velzen, S., Farrar, G. R., Gezari, S., et al. 2011, ApJ, 741, 73
- van Velzen, S., Anderson, G. E., Stone, N. C., et al. 2016, Science, 351, 62
- Weymann, R. J. 1970, ApJ, 160, 31
- Yaron, O., & Gal-Yam, A. 2012, PASP, 124, 668